RSC Advances

PAPER

Cite this: *RSC Adv.*, 2021, **11**, 9721

Fast 3D-lithium-ion diffusion and high electronic conductivity of Li_2MnSiO_4 surfaces for rechargeable lithium-ion batteries

Gamachis Sakata Gurmesa, [ade] Natei Ermias Benti, [f] Mesfin Diro Chaka, [g] Girum Ayalneh Tiruye, [c] Qinfang Zhang, [d] Yedilfana Setarge Mekonnen [*b] and Chernet Amente Geffe[*a]

High theoretical capacity, high thermal stability, the low cost of production, abundance, and environmental friendliness are among the potential attractiveness of Li_2MnSiO_4 as a positive electrode (cathode) material for rechargeable lithium-ion batteries. However, the experimental results indicated poor electrochemical performance in its bulk phase due to high intrinsic charge transfer resistance and capacity fading during cycling, which limit its large-scale commercial applications. Herein, we explore the surface stability and various lithium-ion diffusion pathways of Li_2MnSiO_4 surfaces using the density functional theory (DFT) framework. Results revealed that the stability of selected surfaces is in the following order: (210) > (001) > (010) > (100). Moreover, the Wulff-constructed equilibrium shape revealed that the Li_2MnSiO_4 (001) surface is the most predominant facet, and thus, preferentially exposed to electrochemical activities. The Hubbard-corrected DFT (DFT + U, with U = 3 eV) results indicated that the bulk insulator with a wide band gap (E_g = 3.42 eV) changed into narrow electronic (E_g = 0.6 eV) when it comes to the Li_2MnSiO_4 (001) surface. Moreover, the nudged elastic band analysis shows that surface diffusion along the (001) channel was found to be unlimited and fast in all three dimensions with more than 12-order-of-magnitude enhancements compared with the bulk system. These findings suggest that the capacity limitation and poor electrochemical performance that arise from limited electronic and ionic conductivity in the bulk system could be remarkably improved on the surfaces of the Li_2MnSiO_4 cathode material for rechargeable lithium-ion batteries.

Received 25th January 2021
Accepted 12th February 2021

DOI: 10.1039/d1ra00642h

rsc.li/rsc-advances

1. Introduction

There is growing interest in the large-scale application of dilithium orthosilicate (Li_2MSiO_4, M = Fe, Mn, Co, and Ni) cathode materials[1–3] for rechargeable lithium-ion batteries (LIB) like that of recent developments in anode materials.[4] These are because of their cyclability, thermal stability and polymorphism possibilities over a wide range of temperatures just to mention a few. As a promising cathode material for the next-generation rechargeable LIB, Li_2MSiO_4 cathode materials are extensively investigated *via* both experimental and computational approaches. The designed LIBs from such cathode materials are widely used for portable electronic devices and also for sustainable transportation including electric vehicles (EVs) and plug-in hybrid electric vehicles (PHEVs). They also have significant potential to mitigate the intermittency of renewable energy sources such as solar, wind, and hydroelectric power.[5,6]

Arroyo Dambablo *et al.*[7] computationally studied the effect of the different polyoxyanions composed of $(XO_4)^{n-}$, where X = Ge, Si, As, Sb, and P on Li_2MXO_4 materials based on the relation between the Li^+ deintercalation voltage and their corresponding electronegativity. Their findings indicated the best fit for Li_2MnSiO_4 materials. However, Li^+ deintercalation voltages for Co and Ni silicates were found to be too high for the current electrolyte window. Experimental studies[8,9] also confirmed that Li_2CoSiO_4 and Li_2NiSiO_4 have low capacities and poor reversibility. Li_2MSiO_4 (M = Mn and Fe) are also highly preferable LIB cathode materials compared to other polyanion compounds

[a]*Department of Physics, College of Natural and Computational Sciences, Addis Ababa University, P. O. Box 1176, Addis Ababa, Ethiopia. E-mail: chernet.amente@aau.edu.et*

[b]*Center for Environmental Science, College of Natural and Computational Sciences, Addis Ababa University, P. O. Box 1176, Addis Ababa, Ethiopia. E-mail: yedilfana.setarge@aau.edu.et*

[c]*Materials Science Program/Department of Chemistry, College of Natural and Computational Sciences, Addis Ababa University, P. O. Box 1176, Addis Ababa, Ethiopia*

[d]*School of Materials Science and Engineering, Yancheng Institute of Technology, Yancheng 224051, China. E-mail: qfangzhang@gmail.com*

[e]*Department of Physics, College of Natural and Computational Sciences, Mettu University, P. O. Box 318, Mettu, Ethiopia*

[f]*Department of Physics, College of Natural and Computational Science, Wolaita Sodo University, P. O. Box 138, Wolaita Sodo, Ethiopia*

[g]*Computational Data Science Program, College of Natural and Computational Sciences, Addis Ababa University, P. O. Box 1176, Addis Ababa, Ethiopia*

such as $LiMPO_4$ (M = Fe, Mn, and Co), which are limited to only a single Li^+ insertion and extraction per formula unit.[10,11] Moreover, other layered transition metal oxide cathode materials (for example, $Li_{1/3}Mn_{1/3}Co_{1/3}O_2$) are also toxic and costly.[12]

Previous studies have demonstrated that the method used to synthesize Li_2MnSiO_4 and other polyanion cathode materials also significantly influences their crystal structures, and so does their ionic conductivity.[1,3,13] One of the strategies to improve the electrochemical performance of lithium-ion batteries with Li_2MnSiO_4 is the optimization of the particle size and morphology. Particularly, the rate of electrochemical performance increases with the reduction in the particle size of Li_2MnSiO_4. This is because the porous structure significantly shortens the diffusion time of Li^+ in Li_2MnSiO_4 cathode materials. Therefore, since the orthorhombic structure of Li_2MnSiO_4 has smaller particle size than that of the monoclinic structure, it will have better Li^+ diffusion, resulting in better electrochemical performance.[1,3,13–15] Polymorphs of Li_2MSiO_4 tetrahedral structures are well known to be classified into low- and high-temperature forms, which differ in the distribution of cations within tetrahedral sites of a hexagonal close-packed (HCP)-based arrangement of oxygen. According to the literature, five different structures were observed with Li_2FeSiO_4,[16–19] three as-synthesized (two are orthorhombic, *Pmnb* and $Pmn2_1$; one is monoclinic, $P2_1/n$) and two cycled phases ($Pmn2_1$ cycled and $P2_1/n$ cycled). Similarly, multiple phases have been reported for Li_2MnSiO_4 [2,13,20,21] with two orthorhombic ($Pmn2_1$ and *Pmnb*) and one monoclinic ($P2_1/n$) symmetries; Li_2CoSiO_4 [22–24] has two orthorhombic ($Pnb2_1$ and $Pmn2_1$) and one monoclinic ($P2_1/n$) symmetries, while Li_2NiSiO_4 [3,25,26] has one crystal symmetry.

The structural, electronic and electrochemical properties of Li_2MSiO_4 depend on the distributions of M. The density functional theory (DFT) predicted some parameter variations, for instance, cell, volume and voltage intercalations between intermediate phases (Li_2MSiO_4, $LiMSiO_4$ and $MSiO_4$) based on their crystal symmetry.[27] According to their report, Li_2MnSiO_4 in the orthorhombic symmetry with the $Pmn2_1$ space group was found to be the most stable structure. Due to the double reversible redox state of Mn ions (Mn^{2+}/Mn^{3+} and Mn^{3+}/Mn^{4+}) within the electrochemical stability window of LIB common electrolytes,[28–31] its theoretical energy density reaches as high as 333 mA h g^{-1}.[32] Li_2MnSiO_4 also has a higher operating voltage of 4.8 V against Li^+/Li electrodes with stability of organic electrolytes.[28,30,31] Moreover, the Mn^{4+} is more accessible than Fe^{4+} and Co^{4+}.[33,34] However, the electrochemical performance of Li_2MnSiO_4 has many drawbacks such as the very low Li^+ diffusion coefficient estimated from 10^{-14} to 10^{-16} cm^2 s^{-1} and electronic conductivity from 10^{-12} to 10^{-16} S cm^{-1} at room temperature[35,36] limiting its electrochemical performance. Unlike other polyanion cathode materials, for instance, $LiMPO_4$,[10] bulk Li_2MnSiO_4 supports two-dimensional Li^+ diffusion in its orthorhombic ($Pmn2_1$) symmetry.[20,37,38]

The development of battery nanoelectrodes plays a vital role in achieving higher ionic and electronic transport. These are possible in one way by maximizing fast lithium diffusion pathways and in another way by narrowing electronic bandgaps unlike their corresponding bulk insulator because of the quantum confinement effect.[39–41]

Previous studies have demonstrated the development of Li_2MnSiO_4 cathode materials at nanoscale[13,18,22] with improved charge/discharge kinetics. For instance, a nanostructured Li_2MnSiO_4 material was synthesized[42] by an easy and fast urea combustion method, which showed an extraordinarily intrinsic electronic conductivity of 4 ± 10^{-8} S cm^{-1}. Ultrathin nanosheets of Li_2MnSiO_4 (M = Mn/Fe)[31] were also prepared by a rapid one-pot synthesis method using a mixed solvent of aqueous ethanol, and the results revealed a superior energy density of 340 mA h g^{-1}. Very recently, Ding *et al.* have reported the (100), (010), (001), and (210) facets as stable surface structures of Li_2MnSiO_4 using DFT calculations combined with experimental characterizations.[43] Interestingly, they also managed to successfully synthesize elongated, hexagonal prism-shaped Li_2MnSiO_4@C nanoplates with the preferentially exposed (001) and (210) facets. The initial discharge capacity was estimated as high as 326 mA h g^{-1} that corresponds to 1.98 Li^+ stored PFU of Li_2MnSiO_4, while the charge specific capacity was found to be 367.6 mA h g^{-1}, which is higher than that of bulk Li_2MnSiO_4 (333 mA h g^{-1}) determined by a galvanostatic charge–discharge method. Although the Li^+ diffusion rate (1.0043×10^{-13} cm^{-2} s^{-1}) for Li_2MnSiO_4@C nanoplates was calculated, the kinetic pathways, Li^+ diffusion dimensionalities and electronic structures of preferentially exposed surfaces were not exhaustively emphasized. If the two-dimensional Li^+ diffusion and electronic insulating properties of bulk Li_2MnSiO_4 enhanced to fast three-dimensional Li^+ diffusion and electronic conductive properties, higher electrochemical performances could be achieved in Li_2MnSiO_4 cathode materials for LIBs. The DFT calculation is also a very powerful technique to predict metal–ion and metal–air batteries at bulk, surface, and interface structures emphasizing on the charge (ionic, electronic, and polaronic) transport mechanisms, thermodynamic stability, and their catalytic effect.[15,20,35,44–49]

Herein, we employed the DFT + *U* analysis to investigate the electronic properties, structural stability and lithium-ion diffusion pathways in the bulk and selected surface structures of the Li_2MnSiO_4 cathode material in the rechargeable lithium-ion batteries. Detail analysis will also be given to rationalize the reason behind the superior surface conduction observed on the Li_2MnSiO_4 (001) surface unlike the previously reported poor bulk Li_2MnSiO_4 conductivity.

2. Methodology

A. Bulk crystal structure

Li_2MnSiO_4 crystallizes in two main crystal systems: one is the orthorhombic symmetry of the $Pmn2_1$ and *Pmnb*[21,27,35,50] space groups at low temperatures and the other is the monoclinic symmetry with the *Pn*[51] and $P2_1/n$[52] space groups at high temperatures. These various polymorphs of Li_2MnSiO_4 showed different electrochemical performances due to the variety of Li^+ diffusion pathways through their crystal lattices. Among the four polymorphs, the orthorhombic symmetry with the $Pmn2_1$ space group is widely studied due to its high thermal stability,

although it supports two-dimensional lithium-ion diffusion whereas the monoclinic symmetry is less stable but supports three-dimensional lithium diffusion.[37,38] The unit cell of the $Pmn2_1$ crystal structure was retrieved from the Material Project open database source (see Fig. 1).[53] In the unit cell, the $Pmn2_1$ crystal structure has 16 atoms: Li = 4, Mn = 2, Si = 2 and O = 8 atoms. For the present calculations, we construct a 2 × 2 × 2 supercell, comprising 128 atoms: Li = 32, Mn = 16, Si = 16 and O = 64 atoms. Fig. 1(b) shows the supercell of the Li_2MnSiO_4 crystal structure, while Fig. 1(c) is the corresponding (001) crystal structure to be most emphasized in the subsequent sections. Observing Fig. 1(a) and (b), all the cations are arranged in the tetrahedral complexes of LiO_4, MnO_4, and SiO_4, in which the structure may collapse as hexagonally closely packed oxygen arrays are partially distorted by the Jahn–Teller effect.[54]

B. Surface crystal structures

Li_2MnSiO_4 surface structures were constructed from the bulk supercell with Li–O and Mn–Si–O terminations, especially those experimentally confirmed,[43] namely, (210), (001), (010), and (100) surfaces, were emphasized (Fig. 2). The number of atoms in all surfaces are the same (128) with Li = 32, Mn = 16, Si = 16 and O = 64 atoms. All the Li–O terminated Li_2MnSiO_4 surface structures, namely, (100), (010), and (001) facets are fixed with more than 14 Å vacuum space to get the ground-state energy. The Mn–Si–O terminated Li_2MnSiO_4 (210) surface structure is the thinnest with 5.506 Å among all the surface structures, which is indicative of the inconvenience as an electrochemically active surface, as it is predominantly covered by the other facets.

C. Computational details

Grid-based projector augmented wave method (GPAW) code was implemented to solve electronic-structure problems with the DFT[55,56] framework. The exchange correlations were examined with generalized gradient approximations (GGA) by the Perdew–Burke–Ernzerhof (PBE) functional.[57] The core electrons were treated by the projected-augmented wave (PAW) method.[58] GPAW uses a real space basis set with grid points. The ground-state energies are calculated using grid space fixed at 0.18. With a Monkhorst–Pack grids 2 × 2 × 2 for bulk, 2 × 2 × 1 for the (001) and (210) surfaces, and 2 × 1 × 2 for the (010) surface and 1 × 2 × 2 for the (100) surface. Li_2MnSiO_4 is found to be antiferromagnetic in agreement with the previous reports,[13,27,32] and thus, the magnetic moment for Mn ions is set to be 4. All the

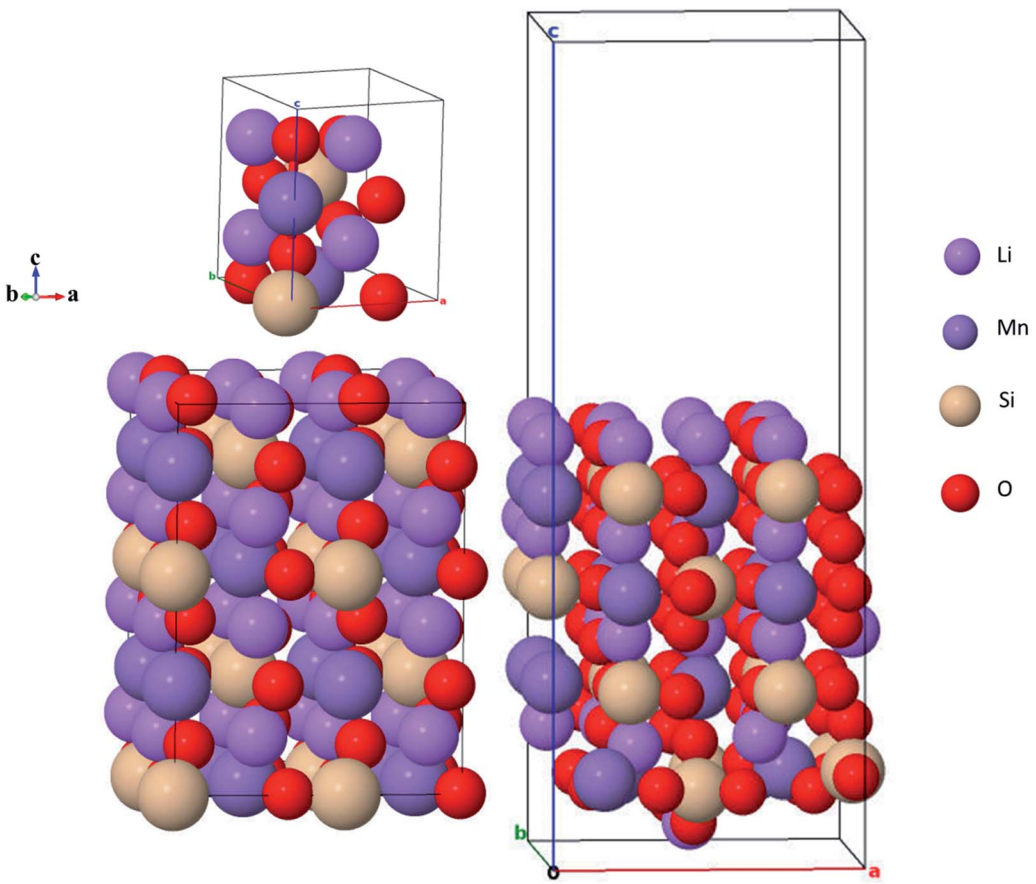

Fig. 1 (a) Unit cell of DFT-optimized Li_2MnSiO_4 structure in the orthorhombic ($Pmn2_1$) symmetry as shown in polyhedral complexes in which all the cations Li, Mn, and Si residing in LiO_4, MnO_4 and SiO_4 form a corner-sharing tetrahedral pyramid. (b) Constructed 2 × 2 × 2 supercell of the Li_2MnSiO_4 structure in the polyhedral symmetry showing all the cations Li, Mn, and Si residing in LiO_4, MnO_4 and SiO_4 complexes forming a corner-sharing tetrahedral pyramid. (c) DFT-optimized Li_2MnSiO_4 (001) surface structure.

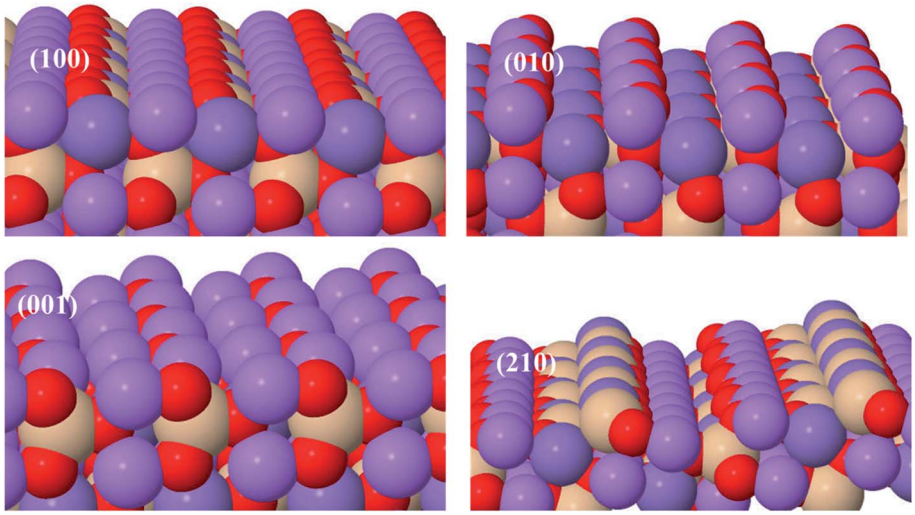

Fig. 2 Structures of low-energy Li_2MnSiO_4 surfaces.

Table 1 Calculated surface free energies of selected Li_2MnSiO_4 surfaces

Orientation	(100)	(010)	(001)	(210)
γ (J m^{-2})	−42.58	−48.98	−48.82	−55.6

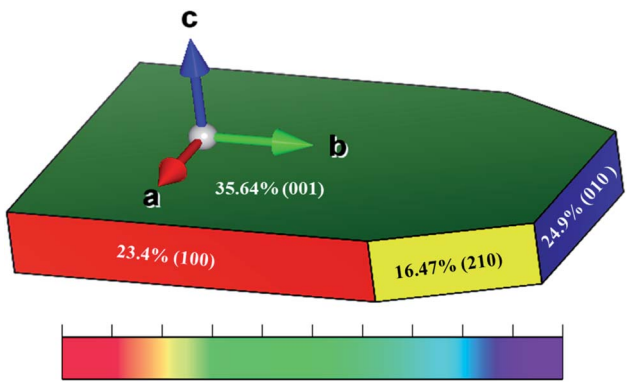

Fig. 3 Wulff-constructed equilibrium shape of Li_2MnSiO_4 based on the calculated relative surface areas and surface free energies.

Table 2 Calculated E_g values with the U value (eV) for the bulk and surface of Li_2MnSiO_4. The corresponding E_g values for the surface are presented inside the parenthesis

U	0	1	1.5	2	2.5	3	3.5	4	4.5	5	5.5	6
E_g	2.5 (0)	2.84	3	3.16	3.29	3.42 (0.6)	3.54	3.64	3.74	3.82	3.89	3.95

structures were relaxed to their ground-state levels by employing spin-polarized calculations until the Hellmann–Feynman forces are less than 0.03 eV A^{-1}. GGA (PBE) often leads to significant deviations from experimental results, in particular the band gap (E_g), due to the incomplete cancellation of the electronic self-interaction energy (SIE) for systems exhibiting a strong localization of the d and/or f-orbital electrons, for instance, Mn(3d) in Li_2MnSiO_4. Previous studies solved this problem[59–61] by employing the appropriate Hubbard correction. For example, U = 3.9 eV was used for Mn(3d), which is not always the case as it also depends on the chemical element incorporated within a particular compound.[59–62] With this consideration, E_g was calculated by varying U-values from 1 to 6 eV with an interval of 0.5. U = 3 eV was found to provide the appropriate E_g and used throughout the calculations. Surface free energies of the selected Li_2MnSiO_4 surface structures were determined using the surface energy equation (eqn (1)):

$$\gamma = \frac{E_{slab} - nE_{bulk}}{2A} \quad (1)$$

where E_{bulk} is the total energy per formula unit of Li_2MnSiO_4, E_{slab} is the total energy of the slab constructed from the supercell containing n formula units of Li_2MnSiO_4 and A is the base area of the slab.

The minimum energy pathway (MEP) and the activation barriers for Li^+ diffusion in Li_2MnSiO_4 were calculated by the climbing-image nudged elastic band (CI-NEB) method.[63] A 2 × 2 × 2 supercell was considered throughout the calculations. For each CI-NEB calculation, five intermediate images were constructed to interpolate the initial and final states along the Li^+ diffusion path. To calculate the energy barrier (E_b), all images and other ions in the supercell were also allowed to relax to its equilibrium position. From the calculated E_b, the Li^+ diffusion rate (r) and Li^+ diffusion coefficient (D) were calculated using the Arrhenius equation, $D = a^2r$ and $r = \nu e^{-E_b/k_BT}$,[45] where a is the minimum jump length of the Li atom from one site to another along the facile channel, e is the electronic charge, ν is the hopping rate, k_B is the Boltzmann constant and T is the temperature. Throughout the present work, $\nu = 10^{13}$ s^{-1}, kB = 8.6173326 × 10^{-5} eV K^{-1}, and T = 298 K were used.

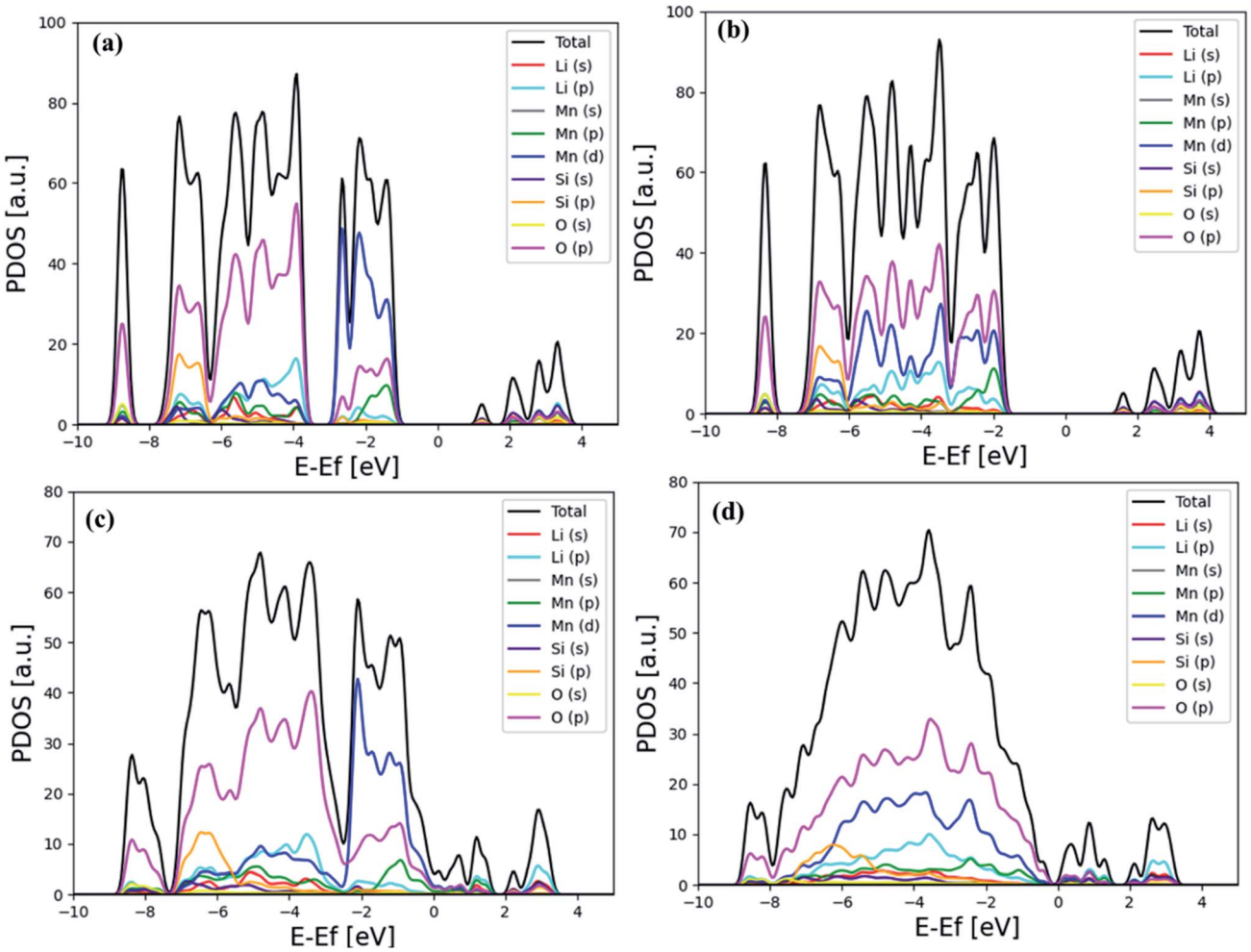

Fig. 4 Calculated PDOS indicated for bulk Li_2MnSiO_4: (a) PBE and (b) PBE + U (at $U = 3$ eV). Calculated PDOS for the Li_2MnSiO_4 (001) surface using (c) PBE and (d) PBE + U (at $U = 3$ eV) functionals.

3. Results and discussion

A. Calculation of surface energies

The structural stability of the selected low index surfaces was identified from the surface free energy calculations by manipulating eqn (1), and the results are summarized in Table 1 and the respective crystal structure facets of Li_2MnSiO_4 are indicated in Fig. 2. The negative sign indicates that the selected surface structures are stable. Among the facets of Li_2MnSiO_4, the (210) surface orientation is the most stable surface with a free energy of about -55.6 J m^{-2}.

The results indicate that the identified surfaces are in the low index facet with their relative decreasing order of surface stability as (210) > (010) > (001) > (100), which is in agreement with the recent experiment.[43]

B. Wulff construction

The Wulff shape for Li_2MnSiO_4 based on the surface free energies in Table 1 is shown in Fig. 3. The green, red, blue, and yellow colors show that the contribution of 35.64, 24.9, 23.4, and 16.47% of a surface by the (001), (010), (100), and (210) facets is based on the Wulff shape-constructed areal surfaces, respectively. These results indicate that all the Li–O terminated surface structures of Li_2MnSiO_4 are better than that of Mn–Si–O terminated surface structures, which is the (210) facet.

In contrast to the calculated surface free energy, the Wulff shape illustrates that the areal surface contributions of the (210) and (100) surfaces are relatively minimum with respect to the formation of facets. The majority of the Wulff shape is dominated by the (001) facet, designated by green color in Fig. 3, with intermediate surface stability, hence limiting wide electrochemical kinetics due to the coverage of an electrochemically active surface area of the (210) facet. Therefore, the (001) facet was selected for further analysis because of the higher surface coverage.

C. Bulk and surface electronic structures

Bulk and surface electronic structures were considered to examine the electronic properties and their influence on the overall electrochemical performance of Li_2MnSiO_4. After relaxations, the total magnetic moments of the bulk and (001) surface structures of anti-ferromagnetic Li_2MnSiO_4 were

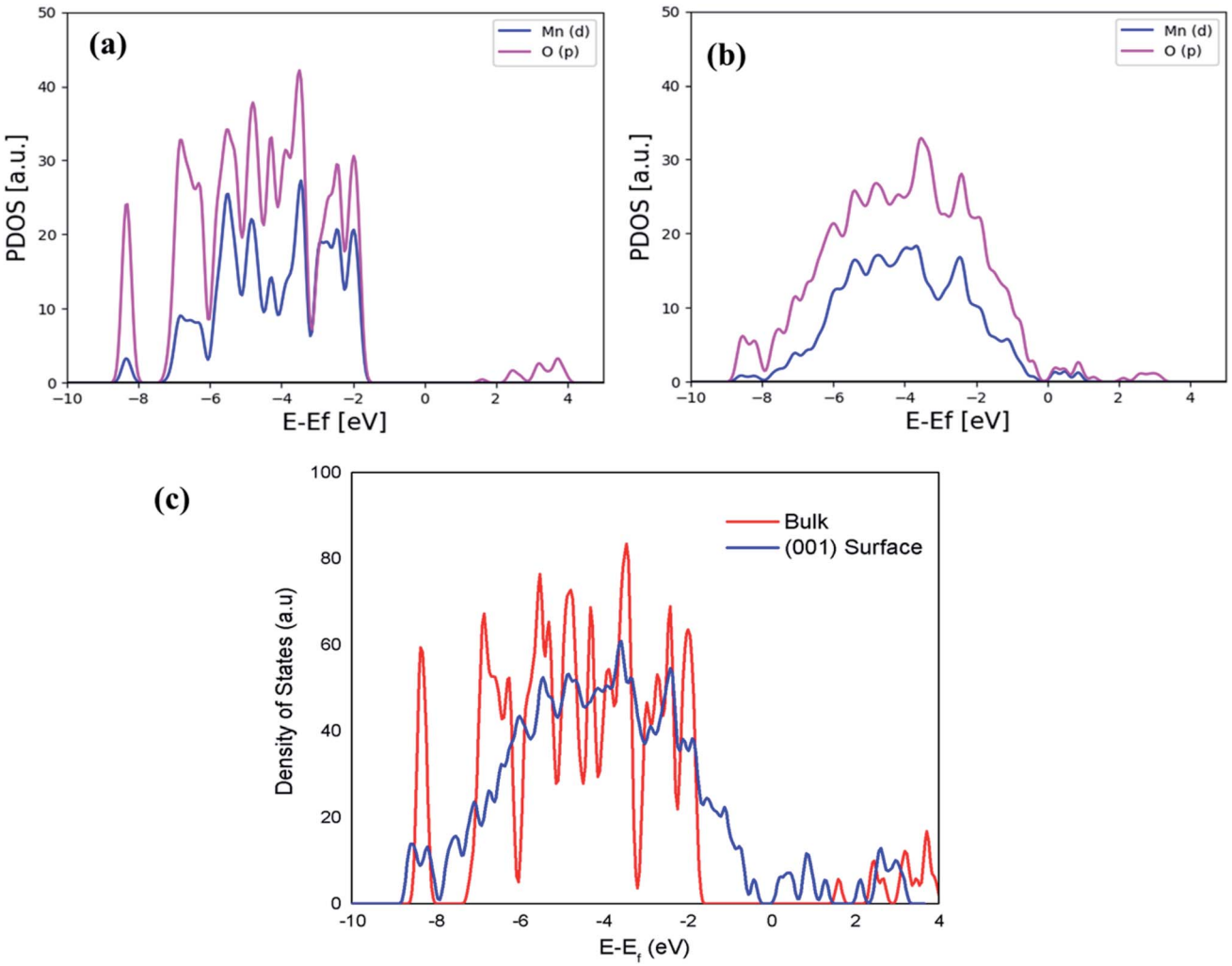

Fig. 5 Calculated PDOS for the most dominant spectra for the bulk (a) and (001) surface (b) separately, while (c) presents a comparison of the calculated DOS for the bulk and (001) surface.

calculated to be 80 and 73.54, respectively. The average magnetic moment for the Mn ion in the bulk and (001) surface of Li_2MnSiO_4 structures were calculated to be 4.43 and 4.17, respectively, slightly decreasing in the surface.

The strongly correlated electrons in the case of d-orbital or f-orbitals of transition metal cathode materials need the Hubbard correction (U) due to electron SIE, otherwise underestimate some calculated parameters when compared with the experimental results, for instance, E_g calculated at the DFT (PBE) theory level. Thus, to calculate reasonable E_g values equivalent to experimental results, one needs to add the Hubbard correction, U (eV).[59–62] Although it is challenging to fix the specific U-value for a particular d- or f-orbital element, researchers used different U-values without clear-cut reasons especially when the experimental result is not found.

To fix this, we used different U-values from 1 to 6 eV with 0.5 intervals in the GPAW code, as clearly indicated in Table 2. For this work, the calculated E_g values were found to be 3.42 and 0.6 eV for the bulk and (001) surface structures of Li_2MnSiO_4, respectively. To the best of our knowledge, there is no experimental or calculated E_g value for Li_2MnSiO_4 using the GPAW code. According to the literature, some reported E_g (eV) values based on the Vienna Ab initio Simulation Package (VASP) code were found for Li_2MnSiO_4 in the range between 2.21 and 3.44 eV.[27,53,64–66] It is obvious that the values of the Hubbard correction used in the VASP code are quite different and higher than the values used in the GPAW code employed in this work. To select the appropriate E_g value for this material, we calculated different E_g values as a function of the Hubbard correction (U-value) about the average E_g reported in previous similar studies, and the results are summarized in Table 2. Accordingly, the U-value of 3 eV is chosen as the appropriate Hubbard correction for both the bulk and surface systems with E_g values of 3.42 and 0.6 eV, respectively.

Fig. 4 shows the detailed analysis of the electronic projected density of state (PDOS) based on PBE and PBE + U functional for the bulk and (001) surface structures of Li_2MnSiO_4. Even though Mn(d) and O(p) orbitals are dominant in both cases, as shown in Fig. 4(a) and (c), their contributions are mixed at the PBE functional, *i.e.* near the Fermi energy level, where the

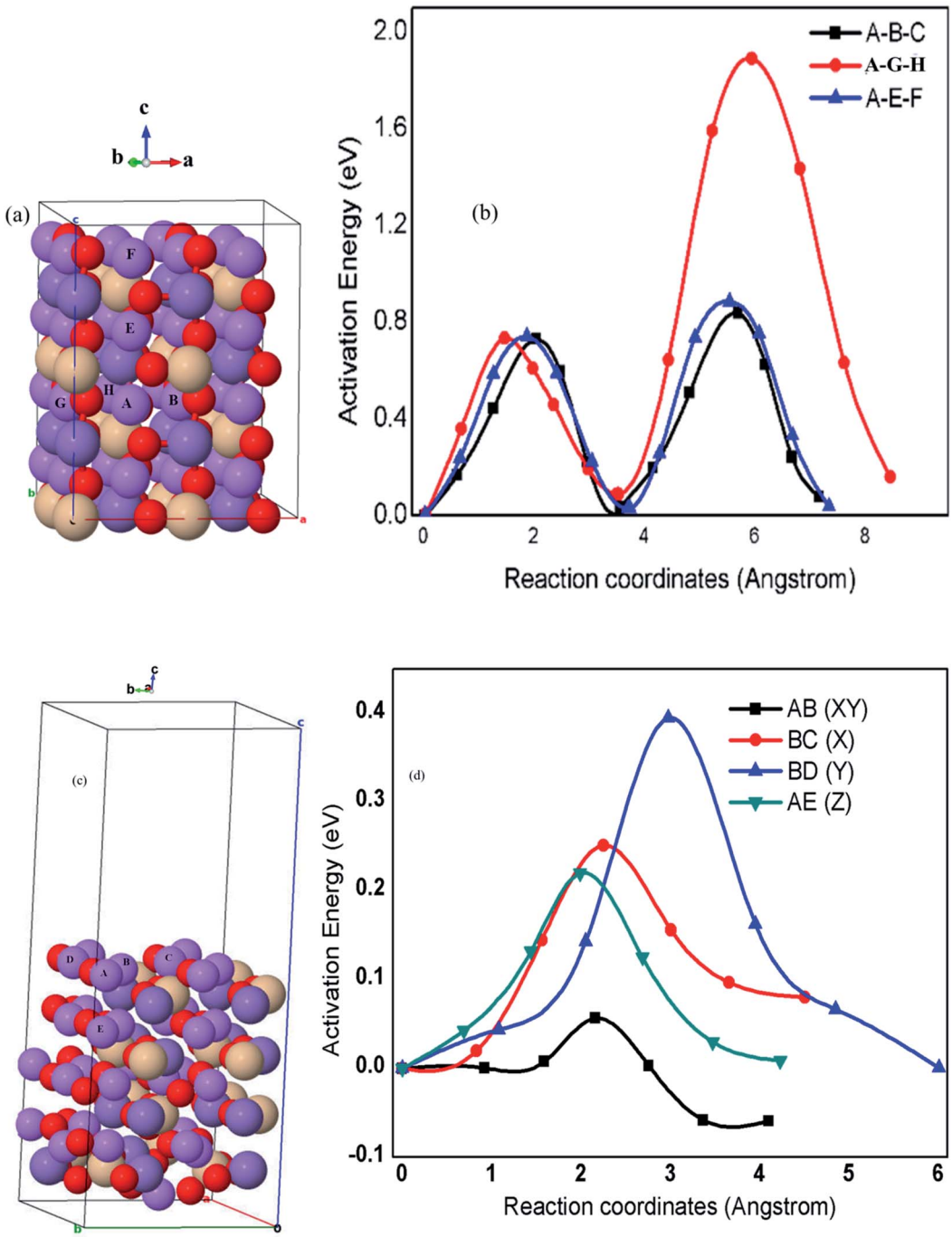

Fig. 6 Proposed pathways for Li^+ and microscopic Li^+ diffusion in bulk (a and b) and (001) surface (c and d) structures of Li_2MnSiO_4, respectively.

contribution of Mn(d) is more dominant, while O(p) becomes dominating as far away in the higher occupied molecular orbital (HOMO) levels.

When the SIE is corrected with the PBE + U functional, the contribution O(p) is more or less uniformly dominant in the lower occupied molecular orbital (LUMO) level. The influence of SIE correction is observed in Fig. 4(b) and (d).

From Fig. 4, it is clearly indicated that O(2p) dominated all the orbitals due to Mn(3d) delocalization, when PBE + U penalty was incorporated in the calculations.

The comparison of dominant spectra PDOS for the bulk and surface is presented in Fig. 5(a) and (b), and it shows that the PDOS of the (001) surface at the Fermi level is more dominant and has exactly metallic properties than the one in the bulk, indicating a higher conductivity as a result of strongly lowering the E_g value of the (001) surface. The calculated E_g value of

Table 3 Calculated E, r and D parameters for the bulk and (001) surface structures of Li_2MnSiO_4

Pathway		a (Å)	E_b (eV)	r (s^{-1})	D (cm^2 s^{-1})
Bulk	AB	3.13	0.73	4.50×10^{-7}	4.40×10^{-15}
	BC	3.13	0.84	6.0×10^{-9}	6.10×10^{-17}
	AE	3.19	0.74	3.50×10^{-7}	3.10×10^{-15}
	EF	3.18	0.88	1.00×10^{-9}	1.30×10^{-17}
	AG	3.13	0.73	4.51×10^{-7}	4.40×10^{-15}
	GH	4.41	1.88	1.60×10^{-19}	3.10×10^{-34}
(001) surface	AB (XY)	4.44	0.06	1.09×10^{12}	2.14×10^{-3}
	BC (X)	3.14	0.25	5.90×10^{8}	5.83×10^{-7}
	BD (Y)	2.94	0.39	2.09×10^{6}	1.81×10^{-9}
	AE (Z)	2.99	0.22	1.90×10^{9}	1.71×10^{-6}

0.6 eV in the (001) surface is due to the contribution of other orbitals, as shown in the total density of states (DOS) of Fig. 5(c). Moreover, it should be very clear here that DFT (GGA at PBE) underestimates electronic E_g in the bulk and surface structures of Li_2MnSiO_4, while DFT + U (PBE + U) calculated E_g in this work is in good agreement with the previous studies.[64,65]

D. Bulk and surface diffusion

The ion diffusion paths and dimensionalities within the crystal structures of cathode materials are among the most important fundamental features and also critical for the charge–discharge rate capabilities.[15] Fig. 6(a), (b) and Table 3 demonstrate the proposed possible kinetic pathways and calculated parameters including the minimum possible lithium atom (Li) hopping distance (a), energy barriers (E_b), diffusion rate (r) and diffusion coefficient (D). The calculated results indicate that bulk lithium-ion diffusion in Li_2MnSiO_4 with the orthorhombic symmetry and $Pmn2_1$ space group is confined to two-dimensional diffusion along the [100] and [001] directions with an estimated diffusion coefficient from 3.12×10^{-15} to 6.09×10^{-17} cm^2 s^{-1}. The corresponding energy barriers are also found to be in the range between $E_b = 0.73$ and $E_b = 0.88$ eV, whilst lithium diffusion along the A–G–H pathway (y-axis) is completely limited mainly in the second half hopping. This is because of the tetrahedral units such as MnO_4 and SiO_4 blocking the Li^+ diffusion channels, resulting in a high energy barrier as high as 1.88 eV that corresponds to very slow diffusion coefficient (3.12×10^{-32} cm^2 s^{-1}) of Li^+ diffusion from the hopping site G to H pathway, as indicated in Fig. 6(a), (b) and Table 3. The calculated results also indicate that the microscopic diffusions following the A–B–C pathway (x-axis) are twice hopping from A to B hopping site (4.4×10^{-15} cm^2 s^{-1}) and from B to C hopping site (6.1×10^{-17} cm^2 s^{-1}) with their corresponding energy barriers (0.73 and 0.84 eV), respectively. The microscopic diffusions follow the A–G–H pathway from A to G (4.4×10^{-15} cm^2 s^{-1}) and G to H (3.1×10^{-34} cm^2 s^{-1}) hopping sites with the calculated energy barriers (0.73 and 1.88 eV), respectively.

Similarly, microscopic diffusion follows the A–E–F pathway (z-axis) from hopping site A to E (3.1×10^{-15} cm^2 s^{-1}) and E to F (1.3×10^{-17} cm^2 s^{-1}) with calculated energy barriers (0.74 and 0.88 eV), respectively. These results indicate that the microscopic diffusion along the (010) direction from hopping site G to H (1.88 eV) is a rate-limiting step during charge/discharge kinetics, which proves that bulk Li_2MnSiO_4 with the orthorhombic symmetry and $Pmn2_1$ space group is truly confined to two-dimensional Li^+ transport pathways, as summarized in Fig. 6 and Table 3.

The calculated E_b in this work is better than the previously reported DFT and atomistic simulation studies,[30,36,38] proving that Li_2MnSiO_4 with the orthorhombic symmetry and $Pmn2_1$ space group supports two-dimensional Li^+ transport. Despite the calculated high energy barriers ($E_b \approx 0.88$ eV) along the (001) and (1000) channels as also reported in other studies, third-dimensional Li^+ diffusion, specifically along the (010) channel following AG and GH paths, has not been reported yet. To optimize unlimited and fast Li^+ transport paths, all the channels along the 3D direction are of paramount importance that we present by surface designing, particularly, on the Li_2MnSiO_4 (001) surface.

The Li_2MnSiO_4 (001) surface was explored to be fast and unlimited Li^+ diffusion, and better electronic conductive surface, which is essential to the higher-power capability of rechargeable Li-ion batteries. For detailed analysis, identified Li^+ diffusion pathways from bulk to the surface (AE) and on the surface (AB, BC, and BD) were emphasized. The DFT calculations show that surface diffusion along the [100], [010], and [001] directions with a dramatically lowered energy barrier (0.057–0.395 eV) corresponds to a higher estimated diffusion coefficient (2.14×10^{-3} to 1.81×10^{-9} cm^2 s^{-1}). Li^+ diffusion paths follow similar mechanisms as discussed in the case of bulk diffusion. In Fig. 6(c), (d) and Table 3, the four microscopic Li^+ diffusion pathways and estimated energy barriers E_b were identified within the surface and from the surface to bulk (see Fig. 6 and Table 3 for details). The calculated E_b value along the AB (XY), BC (X), BD (Y), and AE (Z) pathways were found to be 0.06, 0.25, 0.40, and 0.22 eV, respectively, attributing to the rapid diffusion coefficient estimated to be 1.90×10^{-3} cm^2 s^{-1} (AB), 9.6×10^{-7} cm^2 s^{-1} (BC), 1.6×10^{-9} cm^2 s^{-1} (BD), and 1.8×10^{-6} cm^2 s^{-1} (AE), respectively, enabling higher charge–discharge rates on the Li_2MnSiO_4 (001) surface. The surface conductivity of this work is because of the remarkable results of Fig. 4(d), 5(c), 6(c) and Table 3. On the Li_2MnSiO_4 (001) surface, Li^+ diffusion channels were found to be open and Li^+ diffuses with very minimum energy costs, inducing surface ionic conductors for this material. With regard to the electron conductivity, the Mn cations with d-orbital and O anions with p-orbital strongly overlapped, indicating the Mn(d) and O(p) hybridizations, which facilitates fast electron transfer, inducing a very narrow bandgap energy (0.6 eV) unlike the bulk insulating property (3.42 eV). The results suggest that Li^+ diffusion on the Li_2MnSiO_4 (001) surface is three dimensional and very fast with a diffusion coefficient estimated to be 12 to 17 orders of magnitude higher than that of bulk Li_2MnSiO_4. This is also quite different from other polyanion compounds of LIB cathode materials. For instance, $LiFePO_4$ is the well-known material confined to one-dimensional Li^+ diffusion along the (010) direction in its bulk and (010) surface structures. However, the (010) surface Li^+ diffusion was found to be lower than its bulk

diffusion because of the higher energy barrier along this channel, revealing the surface architecture of the Li_2MnSiO_4 cathode material for high-performance lithium-ion batteries.[67]

4. Conclusion

Herein, we investigated the Li^+ transport paths, electronic structures, and structural stabilities of the Li_2MnSiO_4 bulk and surfaces using both DFT and DFT + U analysis. The results of surface free energies predicted the following order of stability for low index surface: (210) > (010) > (001) > (100) facet. Based on the calculated free surface energies, an equilibrium shape of the Wulff construction was predicted and the relative percentage of exposure was found to be 35.64% for (001), 24.9% for (010), 23.4% for (100), and 16.47% for (210). Unlike the bulk insulator, electronic analysis results revealed that there are superior (001) surface conductivity pathways in Li_2MnSiO_4. Moreover, the NEB calculations confirmed unlimited and fast three-dimensional lithium-ion diffusion on the Li_2MnSiO_4 (001) surface, unlike the corresponding bulk phase due to the large energy barrier. The presence of conductive surface pathways for ion and electron transports along the Li_2MnSiO_4 surfaces could substantially improve the performance of the Li_2MnSiO_4-based rechargeable lithium-ion batteries, paving the way for designing and developing high-performance energy storage devices.

Data availability

The data that support the findings of this study are available within the article.

Conflicts of interest

There are no conflicts to declare.

Acknowledgements

This work was supported by thematic research project (Project no. TR/012/2016 and VPRTT/PY-026/2018/10) funded by Addis Ababa University. Y. S. Mekonnen would like to thank the World Academy of Sciences (TWAS) for supporting this work (Research grants 19-202 RG/CHE/AF/AC_G). G. S. Gurmesa would like to acknowledge Mettu University for sponsorship. Moreover, authors would like to thank Dr Tamiru Teshome for valuable discussions.

References

1 H. N. Girish and G. Q. Shao, *RSC Adv.*, 2015, **5**, 98666.
2 A. R. Armstrong, C. Sirisopanaporn, P. Adamson, J. Billaud, R. Dominko, C. Masquelier and P. G. Bruce, *Z. Anorg. Allg. Chem.*, 2014, **640**, 1043.
3 P. Vajeeston, F. Bianchini and H. Fjellvåg, *Energies*, 2019, **12**, 224.
4 J. Lee, J. Moon, S. A. Han, J. Kim, V. Malgras, Y. U. Heo, H. Kim, S. M. Lee, H. K. Liu, S. X. Dou, Y. Yamauchi, M. S. Park and J. H. Kim, *ACS Nano*, 2019, **13**, 9607.
5 J. R. Croy, A. Abouimrane and Z. Zhang, *MRS Bull.*, 2014, **39**, 407.
6 M. M. Thackeray, C. Wolverton and E. D. Isaacs, *Energy Environ. Sci.*, 2012, **5**, 7854.
7 M. E. Arroyo-de Dompablo, M. Armand, J. M. Tarascon and U. Amador, *Electrochem. Commun.*, 2006, **8**, 1292.
8 C. Lyness, B. Delobel, A. R. Armstrong and P. G. Bruce, *Chem. Commun.*, 2007, 4890.
9 S. Thayumanasundaram, V. S. Rangasamy, J. W. Seo and J. P. Locquet, *Ionics*, 2014, **20**, 935.
10 D. Morgan, A. Van der Ven and G. Ceder, *Electrochem. Solid-State Lett.*, 2004, **7**, 2003.
11 Y. M. Kang, Y. Il Kim, M. W. Oh, R. Z. Yin, Y. Lee, D. W. Han, H. S. Kwon, J. H. Kim and G. Ramanath, *Energy Environ. Sci.*, 2011, **4**, 4978.
12 N. Yabuuchi and T. Ohzuku, *J. Power Sources*, 2003, **119**, 171.
13 M. Bini, S. Ferrari, C. Ferrara, M. C. Mozzati, D. Capsoni, A. J. Pell, G. Pintacuda, P. Canton and P. Mustarelli, *Sci. Rep.*, 2013, **3**, 1.
14 X. L. Wu, L. Y. Jiang, F. F. Cao, Y. G. Guo and L. J. Wan, *Adv. Mater.*, 2009, **21**, 2710.
15 M. S. Islam and C. A. J. Fisher, *Chem. Soc. Rev.*, 2014, **43**, 185.
16 G. Mali, C. Sirisopanaporn, C. Masquelier, D. Hanzel and R. Dominko, *Chem. Mater.*, 2011, **23**, 2735.
17 C. Sirisopanaporn, A. Boulineau, D. Hanzel, R. Dominko, B. Budic, A. R. Armstrong, P. G. Bruce and C. Masquelier, *Inorg. Chem.*, 2010, **49**, 7446.
18 P. Zhang, C. H. Hu, S. Q. Wu, Z. Z. Zhu and Y. Yang, *Phys. Chem. Chem. Phys.*, 2012, **14**, 7346.
19 A. Saracibar, A. Van Der Ven and M. E. Arroyo-De Dompablo, *Chem. Mater.*, 2012, **24**, 495.
20 M. E. Arroyo-DeDompablo, R. Dominko, J. M. Gallardo-Amores, L. Dupont, G. Mali, H. Ehrenberg, J. Jamnik and E. Morán, *Chem. Mater.*, 2008, **20**, 5574.
21 R. J. Gummow, N. Sharma, V. K. Peterson and Y. He, *J. Solid State Chem.*, 2012, **188**, 32.
22 C. Zhang, Z. Chen and J. Li, *Chem. Phys. Lett.*, 2013, **580**, 115.
23 G. He, G. Popov and L. F. Nazar, *Chem. Mater.*, 2013, **25**, 1024.
24 A. R. Armstrong, C. Lyness, M. Ménétrier and P. G. Bruce, *Chem. Mater.*, 2010, **22**, 1892.
25 A. Y. Shenouda and M. M. S. Sanad, *Bull. Mater. Sci.*, 2017, **40**, 1055.
26 K. M. Bui, V. A. Dinh and T. Ohno, *J. Phys.: Conf. Ser.*, 2013, **454**, 012061.
27 M. M. Kalantarian, S. Asgari and P. Mustarelli, *J. Mater. Chem. A*, 2013, **1**, 2847.
28 Q. Cheng, W. He, X. Zhang, M. Li and L. Wang, *J. Mater. Chem. A*, 2017, **5**, 10772.
29 T. Muraliganth, K. R. Stroukoff and A. Manthiram, *Chem. Mater.*, 2010, **22**, 5754.
30 A. Kokalj, R. Dominko, G. Mali, A. Meden, M. Gaberscek and J. Jamnik, *Chem. Mater.*, 2007, **19**, 3633.
31 S. S. Liu, L. J. Song, B. J. Yu, C. Y. Wang and M. W. Li, *Electrochim. Acta*, 2016, **188**, 145.
32 I. Belharouak, A. Abouimrane and K. Amine, *J. Phys. Chem. C*, 2009, **113**, 20733.

33 Y. X. Li, Z. L. Gong and Y. Yang, *J. Power Sources*, 2007, **174**, 528.
34 Z. Gong and Y. Yang, *Energy Environ. Sci.*, 2011, **4**, 3223.
35 R. Dominko, M. Bele, M. Gaberšček, A. Meden, M. Remškar and J. Jamnik, *Electrochem. Commun.*, 2006, **8**, 217.
36 R. Dominko, *J. Power Sources*, 2008, **184**, 462.
37 N. Kuganathan and M. S. Islam, *Chem. Mater.*, 2009, **21**, 5196.
38 C. A. J. Fisher, N. Kuganathan and M. S. Islam, *J. Mater. Chem. A*, 2013, **1**, 4207.
39 J. Maier, *Materials for Sustainable Energy: A Collection of Peer-Reviewed Research and Review Articles from Nature Publishing Group*, 2010, vol. 4, p. 160.
40 P. G. Bruce, B. Scrosati and J. M. Tarascon, *Angew. Chem., Int. Ed.*, 2008, **47**, 2930.
41 S. Bashir, P. Hanumandla, H. Y. Huang and J. L. Liu, Nanostructured Materials for Next-Generation Energy Storage and Conversion, *Fuel Cells*, 2018, **4**, 517.
42 P. Chaturvedi, A. Sil and Y. Sharma, *Solid State Ionics*, 2016, **297**, 68.
43 Z. Ding, Y. Feng, D. Zhang, R. Ji, L. Chen, D. G. Ivey and W. Wei, *ACS Appl. Mater. Interfaces*, 2018, **10**, 6309.
44 Y. S. Meng and M. E. Arroyo-De Dompablo, *Energy Environ. Sci.*, 2009, **2**, 589.
45 S. Loftager, J. M. García-Lastra and T. Vegge, *J. Phys. Chem. C*, 2016, **120**, 18355.
46 M. D. Radin, J. F. Rodriguez, F. Tian and D. J. Siegel, *J. Am. Chem. Soc.*, 2012, **134**, 1093.
47 Y. S. Mekonnen, K. B. Knudsen, J. S. G. Mýrdal, R. Younesi, J. Højberg, J. Hjelm, P. Norby and T. Vegge, *J. Chem. Phys.*, 2014, **140**, 1.
48 N. E. Benti, Y. S. Mekonnen, R. Christensen, G. A. Tiruye, J. M. Garcia-Lastra and T. Vegge, *J. Chem. Phys.*, 2020, **152**, 1.
49 N. E. Benti, G. A. Tiruye and Y. S. Mekonnen, *RSC Adv.*, 2020, **10**, 21387.
50 C. Deng, S. Zhang, B. L. Fu, S. Y. Yang and L. Ma, *Mater. Chem. Phys.*, 2010, **120**, 14.
51 H. Duncan, A. Kondamreddy, P. H. J. Mercier, Y. Le Page, Y. Abu-Lebdeh, M. Couillard, P. S. Whitfield and I. J. Davidson, *Chem. Mater.*, 2011, **23**, 5446.
52 V. V. Politaev, A. A. Petrenko, V. B. Nalbandyan, B. S. Medvedev and E. S. Shvetsova, *J. Solid State Chem.*, 2007, **180**, 1045.
53 A. Jain, S. P. Ong, G. Hautier, W. Chen, W. D. Richards, S. Dacek, S. Cholia, D. Gunter, D. Skinner, G. Ceder and K. A. Persson, *APL Mater.*, 2013, **1**, 011002.
54 P. Babbar, B. Tiwari, B. Purohit, A. Ivanishchev, A. Churikov and A. Dixit, *RSC Adv.*, 2017, **7**, 22990.
55 J. Enkovaara, C. Rostgaard, J. J. Mortensen, J. Chen, M. Dułak, L. Ferrighi, J. Gavnholt, C. Glinsvad, V. Haikola, H. A. Hansen, H. H. Kristoffersen, M. Kuisma, A. H. Larsen, L. Lehtovaara, M. Ljungberg, O. Lopez-Acevedo, P. G. Moses, J. Ojanen, T. Olsen, V. Petzold, N. A. Romero, J. Stausholm-Møller, M. Strange, G. A. Tritsaris, M. Vanin, M. Walter, B. Hammer, H. Häkkinen, G. K. H. Madsen, R. M. Nieminen, J. K. Nørskov, M. Puska, T. T. Rantala, J. Schiøtz, K. S. Thygesen and K. W. Jacobsen, *J. Phys.: Condens. Matter*, 2010, **22**(25), 253202.
56 M. Ernzerhof and G. E. Scuseria, *Theor. Chem. Acc.*, 2000, **103**, 259.
57 W. Kohn and J. Sham, *Phys. Rev. B*, 1965, **140**, A1133.
58 P. E. Bloechl, *Phys. Rev. B*, 1994, **50**, 17953.
59 L. Wang, T. Maxisch and G. Ceder, *Phys. Rev. B*, 2006, **73**, 1.
60 N. J. Mosey and E. A. Carter, *Phys. Rev. B*, 2007, **76**, 1.
61 A. Jain, G. Hautier, C. J. Moore, S. Ping Ong, C. C. Fischer, T. Mueller, K. A. Persson and G. Ceder, *Comput. Mater. Sci.*, 2011, **50**, 2295.
62 H. Zhao, X. Wu, Y. Li, J. Shen and J. Xu, *J. Chin. Ceram. Soc.*, 2011, **39**, 1084–1089.
63 G. Henkelman and H. Jónsson, *J. Chem. Phys.*, 2000, **113**, 9978.
64 G. Zhong, Y. Li, P. Yan, Z. Liu, M. Xie and H. Lin, *J. Phys. Chem. C*, 2010, **114**, 3693.
65 S. Q. Wu, Z. Z. Zhu, Y. Yang and Z. F. Hou, *Comput. Mater. Sci.*, 2009, **44**, 1243.
66 M. Y. Arsent'ev, P. A. Tikhonov and M. V. Kalinina, *Glass Phys. Chem.*, 2018, **44**, 455.
67 G. K. P. Dathar, D. Sheppard, K. J. Stevenson and G. Henkelman, *Chem. Mater.*, 2011, **23**, 4032.